International Journal of Neural Systems, Vol. 26, No. 3 (2016) 1650012 (16 pages)

DOI: 10.1142/S012906571650012X

World Scientific
www.worldscientific.com

Reduction of Delay in Detecting Initial Dips from Functional Near-Infrared Spectroscopy Signals Using Vector-Based Phase Analysis

Keum-Shik Hong*
School of Mechanical Engineering
Pusan National University; 2 Busandaehak-ro
Geumjeong-gu, Busan 46241, Korea
kshong@pusan.ac.kr

Noman Naseer†
Department of Cogno-Mechatronics Engineering
Pusan National University; 2 Busandaehak-ro
Geumjeong-gu, Busan 46241, Korea
noman@pusan.ac.kr

Accepted 7 January 2016
Published Online 9 March 2016

In this paper, we present a systematic method to reduce the time lag in detecting initial dips using a vector-based phase diagram and an autoregressive moving average with exogenous signals (ARMAX) model-based q-step-ahead prediction algorithm. With functional near-infrared spectroscopy (fNIRS), signals related to mental arithmetic and right-hand clenching are acquired from the prefrontal and left primary motor cortices, respectively. The interrelationship between oxygenated hemoglobin, deoxygenated hemoglobin, total hemoglobin and cerebral oxygen exchange are related to initial dips. Specifically, a threshold value from the resting state hemodynamics is incorporated, as a decision criterion, into the vector-based phase diagram to determine the occurrence of initial dips. To further reduce the time lag, a q-step-ahead prediction method is applied to predict the occurrence of the dips. A combination of the threshold criterion and the prediction method resulted in the delay time of about 0.9 s. The results demonstrate that rapid detection of initial dip is possible and therefore can be used for real-time brain–computer interfacing.

Keywords: Initial dip; functional near-infrared spectroscopy; vector-based phase analysis; reduction of detection time; prefrontal cortex; motor cortex.

1. Introduction

This paper presents a systematic way of detecting initial dips appearing in functional near-infrared spectroscopy (fNIRS) signals.[1–3] The initial dip denotes the decrease of oxygenated hemoglobin (HbO) caused by a neuronal activation. It is a direct indication of the generation of a neuronal command (i.e., a metabolic signal, not a blood volume related signal). For fast brain–computer interface (BCI), immediate detection of a brain command is crucial. This can be done by detecting the metabolic signal associated with the given command, rather than the blood volume related signal that appears in a while. The initial dip as a metabolic phenomenon has been an important research issue. In relation to its detection, the pioneering works of Kato and his coworkers (see Sec. 2.1 below) have resulted in the vector-based phase analysis method. In their works, however, a systematic way of detecting the occurrence of an initial dip was unclear. In this paper,

*Corresponding author.
†Current address: Department of Mechatronics Engineering, Air University, Sector E-9, Islamabad, Pakistan.

to detect neuronal-command-related initial dips, a novel scheme by combining the vector-based phase analysis method, a threshold-value criterion, and a prediction method based upon an autoregressive moving average with exogenous signals (ARMAX) model is proposed. For demonstration, mental arithmetic and hand-clenching tasks in the prefrontal and motor cortices, respectively, are performed.

fNIRS is a relatively new noninvasive brain-imaging modality that is used to measure the hemodynamic changes, that is, changes in the concentrations of HbO and deoxygenated hemoglobin (HbR). It uses light in the near-infrared range (650–900 nm)[1–3] in which the absorption of light due to skin, tissues, and bones is much lower than that of HbO and HbR. Due to the differences in the absorption spectra of HbO and HbR in the near-infrared range, their relative concentration changes can be measured using light attenuation at multiple wavelengths.

fNIRS utilizes near-infrared light emitter-detector pairs. The emitter emits light at two or more distinct wavelengths. Such light, due to its low absorption by skin and tissues, can penetrate a subject's scalp, traveling inside the skull and causing multiple scatterings of photons. Some of these photons are absorbed, whereas others continue to disperse and pass through the cortical areas wherein the HbO and HbR chromophores absorb the light with different absorption coefficients. A part of photons then exit and are captured using suitably placed detectors. The intensity of the exited light is then used to calculate the HbO and HbR concentration changes along the photon path according to the modified Beer–Lambert law (see Sec. 2.5). The principle of fNIRS measurement, first reported by Kato *et al.*,[1,4] has been applied not only to the study of cerebral hemodynamics for more than two decades now, but also, in more recent years, in the fields of brain mapping, brain-state decoding, and BCI.[5–20] The major advantages of using fNIRS are noninvasiveness, low cost, portability, and ease of use. fNIRS, moreover, because it is an optical modality, produces measurements that are not susceptible to electrogenic artifacts.

The main drawback of using hemodynamics is that it lags the neuronal activation by approximately 2 s.[19,21] In this paper, we attempt to cope with this problem by detecting the initial dip, which occurs ahead of the conventional hemodynamic response. As a result of a task-related event/activity,[22] the oxygen demand in the task-specifically related brain region changes. This causes the concentration changes of oxygenated (ΔHbO) and deoxygenated hemoglobin (ΔHbR) in that region. The dynamics of these concentration changes were also discovered by the optical imaging technique, which revealed that the typical HbR concentration change consists of a small rise in the initial state, peaking up at approximately 2 s, followed by a decrease that endures several seconds after the end of the stimulation.[23,24] This initial rise of ΔHbR has been interpreted as a transient increase due to the metabolism that precedes the conventional hemodynamic response. The metabolism increase makes an increase in ΔHbR concentration and further causes the neurons to draw more oxygen out of the capillary network. Such hemodynamic response eventually overcompensates the initial oxygen demand, resulting in a net increase in HbO concentration. Since an increase in ΔHbR leads to a decrease in the magnetic resonance signal, this initial phase is commonly known, within the functional magnetic resonance imaging (fMRI) community, as the initial dip.[25] This initial dip, either in invasive human/animal studies or in noninvasive human studies, has been reported to occur prior to the increase of blood oxygenation.[2,24–30] However, given its small amplitude and short duration, it has been difficult to detect it. Kato[27] was the first fNIRS study viewing the initial dip from a capillary event. However, they did not use the terminology "initial dip" in their work. Instead, the phenomenon was described as fast-oxygen response in capillary event (FORCE). In fNIRS studies, to the best of the authors' knowledge, the term "initial dip" was first used in Ref. 21 (p. 485) showing a decrease in ΔHbO and an increase in ΔHbR in the visual cortex. Yoshino and Kato[31] classified five types of initial dips using the vector approach, which was the first introduction of multiple types of initial dips. Although the hyperemic phase (increased ΔHbO) would be the main focus in both fMRI and fNIRS studies, the initial phase is believed to reflect more directly the metabolic response and thereby the neuronal activity. The ΔHbO and the change in total hemoglobin (ΔHbT) responses, as concurrent with increased ΔHbR, have varied in the previous studies, which was discussed in detail in Ref. 31.

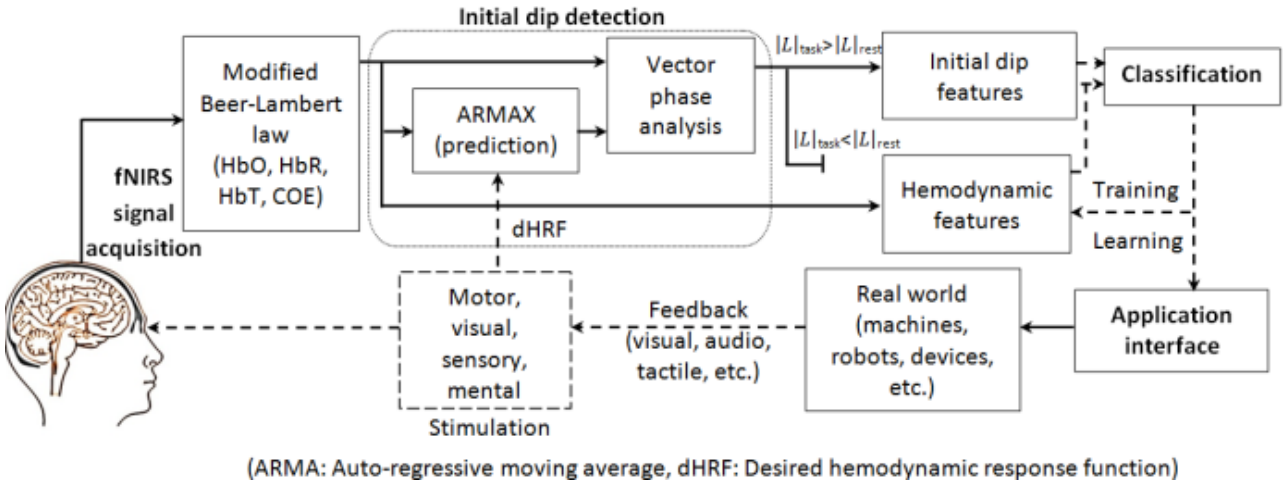

Fig. 1. Application of initial dips for BCI.

The main reason why neuroscientists are so keen in an initial dip is that it is faster than the conventional hemodynamic response, and also more spatially specific.[32–35] This advantage comes from the fact that, in theory, the initial dip is more closely related to the region of neural metabolism and thus can allow for more precise spatial localization than the conventional hemodynamic response can predict. Furthermore, one of the challenges in using fNIRS for BCI purposes is to reduce the inherent delay in the conventional hemodynamic response. Therefore, the development of a new technique for the detection of initial dips and a further reduction of the detection time are necessary in order to use fNIRS for real-time BCI, see Fig. 1.

In this paper, we utilize the vector-based phase analysis of fNIRS signals to detect the initial dip in the prefrontal and motor cortex areas as a result of mental arithmetic and hand-clenching tasks, respectively. We found a time lag in detection of the initial dip, and as a way of reducing the detection time, we applied an autoregressive moving-average model, using a q-step-ahead prediction algorithm to predetermine the occurrence of the initial dip.

The key contributions of this paper towards the realization of real-time BCI lie in the utilization of the vector-based phase diagram, the design of decision criteria, and the implementation of a prediction algorithm. Besides the quickness of detection, the efficiency and accuracy of the proposed method are additional contributions.

2. Methods

The previous NIRS studies,[2,27] in attempting to detect the initial dip, have looked for deoxygenation based on an ΔHbR increase and ΔHbO decrease. Herein, we consider all four indices: ΔHbO, ΔHbR, ΔHbT, and changes in cerebral oxygen exchange (ΔCOE). ΔCOE, defined as the difference between ΔHbR and ΔHbO, is an indicator of oxygenation-level changes in blood vessels, and therefore reflects neuronal activity.[28,36,37] An increase in ΔCOE represents deoxygenation in the capillaries as a result of oxygen consumption by the nerve cells; such increase, therefore, indicates hypoxic change in the blood vessels. A decrease in ΔCOE shows that there is a high level of oxygenation in the blood vessels because oxygen-containing red blood cells are being supplied from the arteries. ΔCOE provides a higher degree of precision as a physiological indicator of increased brain functionality as compared to the conventionally used ΔHbO or HbT.[36,37] In consideration of the four indices of oxygen-level changes, there are four possible cases of hypoxic change, defined as follows.[31]

Case 1. Increase in all ΔHbO, ΔHbR, ΔHbT, and ΔCOE such that the magnitude of ΔHbR is greater than that of ΔHbO. This will result in an increase in ΔCOE, which indicates deoxygenation.

Case 2. A decrease in ΔHbO and increases in ΔHbR, ΔHbT, and ΔCOE. In this case, ΔHbR is positive and ΔHbO is negative, implying that ΔCOE is positive, which indicates deoxygenation.

Case 3. Decrease in ΔHbO and ΔHbT, and increase in ΔHbR and ΔCOE. It is the same as Case 2 except that ΔHbT decreases.

Case 4. Decrease in ΔHbO, ΔHbR, and ΔHbT and increase in ΔCOE. In this case, ΔHbR, ΔHbO, and ΔHbT decrease such that the magnitude of ΔHbR is greater than that of ΔHbO, which results in an increase in ΔCOE.

To examine the behavior of all four indices simultaneously on a single plane, the vector-based phase analysis is used.

2.1. *Vector-based phase analysis*

The vector-based phase analysis method, devised by Kato,[28,31,37,38] is based on an orthogonal vector coordinate plane defined by ΔHbO and ΔHbR signals, as shown in Fig. 2. Rotating this plane by 45° counterclockwise results in another orthogonal plane defined by ΔHbT and ΔCOE such that

$$\Delta\mathrm{HbT} = (\Delta\mathrm{HbO} + \Delta\mathrm{HbR})/\sqrt{2}, \quad (1)$$

$$\Delta\mathrm{COE} = (\Delta\mathrm{HbR} - -\Delta\mathrm{HbO})/\sqrt{2}. \quad (2)$$

The magnitude and the phase of a vector, L, on this plane can be described as

$$|L| = \sqrt{\Delta\mathrm{HbO}^2 + \Delta\mathrm{HbR}^2}, \quad (3)$$

$$E = \tan^{-1}\frac{\Delta\mathrm{COE}}{\Delta\mathrm{HbT}} = \tan^{-1}\frac{\Delta\mathrm{HbR}}{\Delta\mathrm{HbO}} - 45^\circ, \quad (4)$$

where E is a function of the ratio of ΔCOE and ΔHbT,[36] and, therefore, defines the degree of oxygen exchange.[38] The classification of different phases shown in Fig. 2 is also determined by angle E. From the ratios between ΔHbO, ΔHbR, ΔHbT, and ΔCOE, the state of neural activity can be divided into eight phase types on the vector plane (see Fig. 2). By drawing the vector L on the vector-phase diagram, we can see in which phase it lays. Thereby, brain activity can be evaluated qualitatively, as classified into eight different regions in the plane. Previously, a brain-activity evaluation was based upon relative magnitudes only (i.e. the changes in signal amplitude was used). Another advantage of the vector-based phase analysis is that it enables a visualization of the interrelationship of four different indices on a single plane in relation to an evoked brain activity. In the phase diagram, Cases 1–4 described above correspond to Phases 1–4 in Fig. 2, respectively, and the HbX trajectories can be clearly visualized on the plane.

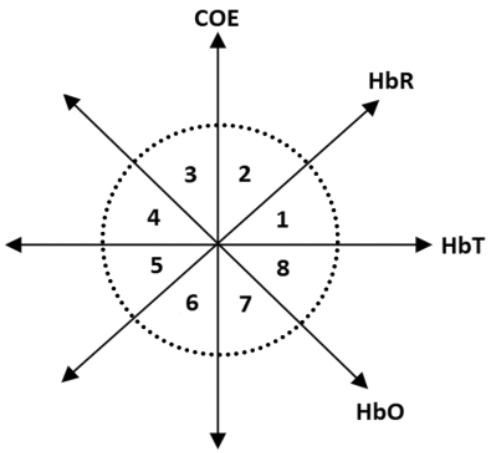

Fig. 2. Vector-based phase diagram: Initial dips occur through Phases 1–4[28,31] when trajectories deviate the (dotted) threshold circle obtained from the resting state.

Our criteria of detecting initial dips are: (i) The vector must lie in any of Phases 1–4 and the magnitude should deviate a certain threshold value that is represented by a dotted circle in the vector-phase diagram. (ii) The radius of this circle is set to the largest value of $|L|$, calculated by Eq. (3), for each channel, during the resting state. By low-pass filtering, the occurrence of an abrupt peak during the resting state can be eliminated in advance.

The reason for using a threshold circle in this study, primarily, is to minimize a false detection of the initial dips. If there is no threshold value for detecting it, some large variations of ΔHbO, ΔHbR values in the resting state and even during the task period could be interpreted as initial dips. For instance, the rise of ΔCOE above zero which is merely a resting state fluctuation can be interpreted as an initial dip.

2.2. *Subjects*

To demonstrate the signal processing scheme, two right-handed male adults participated in the experiments (the role of the second subject was to re-confirm the proposed methodology). Both participants were healthy and had no history of any psychiatric or neurological disorder. The subjects had normal or corrected-to-normal vision. Verbal consent was obtained prior to their enrollment in the experiments and after they were informed in detail about the experimental procedure. The experiments

were conducted in accordance with the Declaration of Helsinki.[39]

2.3. *Experimental protocol*

Two different experiments were performed to illustrate the proposed scheme: mental arithmetic and right-hand clenching.

2.3.1. *Mental arithmetic task*

The participants were seated in a comfortable chair approximately 65–70 cm from a monitor that was used to provide visual cues. They were advised to relax and restrict their head movement as much as possible. Figure 3(a) shows the experimental sequence for the mental arithmetic experiment: the first 15 and the final 7 min were the resting periods; between these, 20 s task-rest sequences were repeated five times. For the mental arithmetic task, the subjects were asked to perform a series of mental calculations of arithmetic problems that appeared on the screen. During the task period, the subjects were asked to subtract a two-digit number (between 10 and 20) from a three-digit number for 10 s, which appeared randomly on the screen. For example, for an initial 3-digit number 730, the sequential messages on the screen were $730 - 17 = ?, 713 - 12 = ?, 701 - 15 = ?$, and so on.[40–47] Since the monitor was turned to black to indicate the end of the arithmetic task, the subject did not go beyond 10 s on each trial.

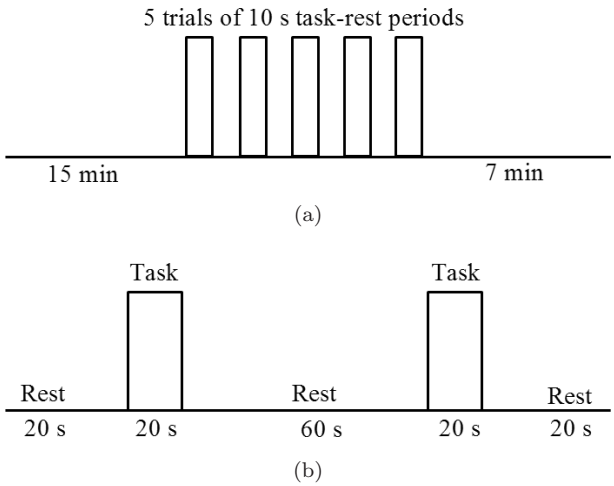

Fig. 3. Experimental paradigms: (a) Mental arithmetic experiment consists of a 15 min rest period followed by five trials of 10 s mental arithmetic task which were followed by a 7 min rest period; (b) hand clinching experiment consists of two 20 s trials with a rest period of 60 s between them.

2.3.2. *Hand-clenching task*

Figure 3(b) illustrates the experimental sequence of the hand-clenching task: the first 20 s was a rest period followed by a 20 s task period; a 1 min rest period was provided before the second trial to allow the signals to settle down to the baseline. Since the brain area in Fig. 4(b) for the hand-clenching task covers the dominant region in the motor cortex and elicits a strong hemodynamic response, it was used to obtain fNIRS signals. During the hand-clenching task, the subjects were advised to clench their right hand with a frequency of approximately 1 Hz. Audio cues "start" and "stop" were given to let the subject know the start and the end of each trial.

2.4. *Optode placement and channel configuration*

The configuration/placement of optodes plays an important role in fNIRS measurement. The emitter-detector distance is determined based on the depth of the region of interest: An increase in emitter-detector distance, for example, leads to an increase in imaging depth.[48–52]

To measure the hemodynamic response signals from the motor cortex and the prefrontal cortex, an emitter-detector separation of 3 cm has been arranged,[50,51] as a separation of more than 5 cm might result in weak and unusable signals.[49] To measure the hemodynamic signals in relation to right-hand clenching, four near-infrared light emitters and five detectors were placed over the primary motor cortex in the left hemisphere. In the mental arithmetic experiment, three emitters and eight detectors were positioned over the prefrontal cortex to measure the signals induced by the mental arithmetic tasks. Figure 4 shows the emitter-detector arrangements in the primary motor and prefrontal cortices.

2.5. *Signal acquisition and processing*

The mental arithmetic signals were acquired using NIRScout from NIRx Medical Technologies, NY, at a sampling rate of 7.81 Hz. The system uses two wavelengths of 760 and 850 nm. The task starting time has been automatically synchronized in the

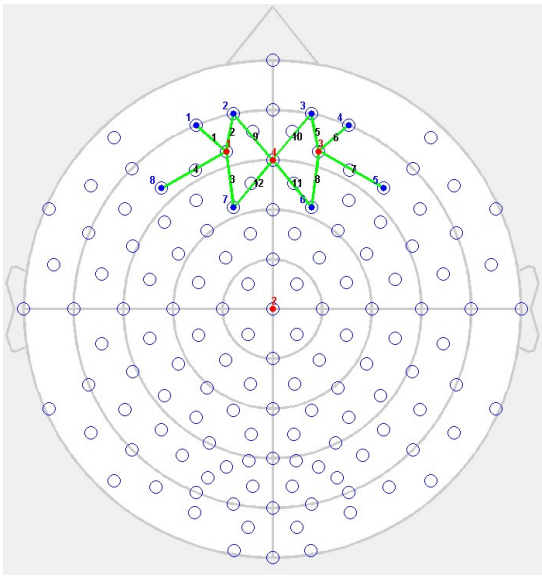

(a)

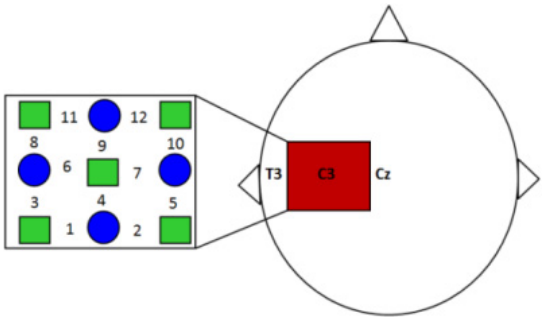

(b)

Fig. 4. Optode placement and channel configuration: (a) For the mental arithmetic task; (b) for the hand clenching task. The emitter-detector distance of 3 cm was applied for both experiments.

fNIRS data by the machine itself. Therefore, if an initial dip is detected, such a human delay that occurs when the subject begins to calculate the arithmetic problems late upon the pop-up of the problems on the screen will be included in the initial dip delay. But, to acquire the initial dip from a hand clenching trial, a multichannel continuous-wave fNIRS system (DYNOT: DYnamic Near-infrared Optical Tomography, two wavelengths of 760 and 830 nm) from the same company, NIRx, NY, was used at a sampling rate of 1.81 Hz. In this case, the starting time has been marked manually in the data.

The raw optical density signals from both machines were first converted to ΔHbO and ΔHbR using the modified Beer–Lambert law.[53]

$$\begin{bmatrix}\Delta\mathrm{HbO}(t)\\ \Delta\mathrm{HbR}(t)\end{bmatrix} = \begin{bmatrix}\alpha_{\mathrm{HbO}}(\lambda_1) & \alpha_{\mathrm{HbR}}(\lambda_1)\\ \alpha_{\mathrm{HbO}}(\lambda_2) & \alpha_{\mathrm{HbR}}(\lambda_2)\end{bmatrix}^{-1} \times \begin{bmatrix}\dfrac{\Delta A(t,\lambda_1)}{d(\lambda_1)}\\ \dfrac{\Delta A(t,\lambda_2)}{d(\lambda_2)}\end{bmatrix} \frac{1}{l}, \quad (5)$$

where $\Delta A(t,\lambda_j)(j = 1,2)$ is the measured absorbance (optical density) variation of a light emitter of wavelength λ_j at time t, $\alpha_{\mathrm{HbX}}(\lambda_j)$ is the extinction coefficient of $\mathrm{HbX}(t)$ in $\mu\mathrm{M}^{-1}\mathrm{mm}^{-1}$, $d(\lambda_j)$ is differential path-length factor (DPF), l is the distance (in millimeters) between the emitter and the detector. The quotient $\Delta A(t,\lambda_j)/d(\lambda_j)$ is unit less. The physiological noises due to respiration, heartbeat, and Mayer waves were then minimized by low-pass filtering of the data with a cut-off frequency of 0.3 Hz. The effect of low-frequency drift, meanwhile, was minimized by high-pass-filtering the data with a cut-off frequency of 0.01 Hz.

Subsequently, ΔHbT, ΔCOE, L, and E were calculated using Eqs. (1)–(4), respectively. Note that L has the same unit as of the four indices whereas E is in degree. The resulting vectors at each data point were calculated from the onset of the task period up to 20 s for all trials and channels. The detection of an initial dip is concluded if a vector L lies in Phases 1–4 in Fig. 2 and its magnitude (i.e. $|L|_{\mathrm{task}}$) begins to deviate from the threshold circle, which is the highest value of $|L|$ at rest (i.e. $|L|_{\mathrm{rest}}$).

3. Results

3.1. *Mental arithmetic experiment*

The time series of ΔHbO, ΔHbR, ΔHbT, and ΔCOE for the activated channels 2, 5, and 10 in all five trials of the mental arithmetic task for Sub. 1 are plotted in Fig. 5. The vector-based phase diagrams of all 12 channels for the first trial is shown in Fig. 6. It can be seen that the vectors corresponding to the first few data points appear in the initial dip phase (Case 4) showing early deoxygenation and then moving to the conventional stage of increased ΔHbO and decreased ΔHbR. It is also apparent that the vectors corresponding to the inactive channels remain within the threshold circle, where the radii of the threshold circles vary per channel since it was set to the highest value during the resting state on that channel.

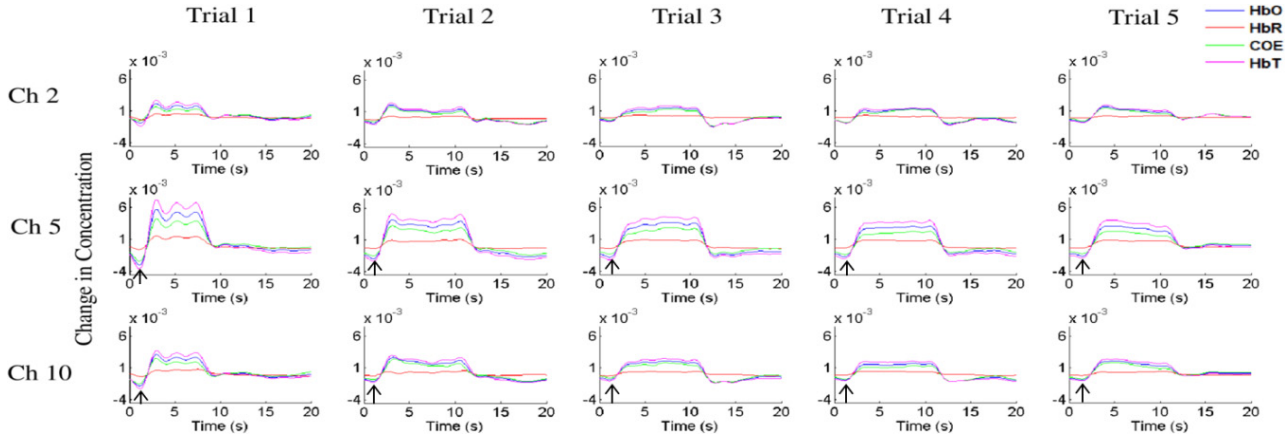

Fig. 5. Time series (ΔHbO, ΔHbR, ΔHbT, ΔCOE) for 20 s after the stimulus for all five trials of the mental arithmetic task (Subject 1). The task duration is from 0 to 10 s. The detection times of initial dips are marked by arrows. Initial dips are not detected in Ch. 2, while they are detected in Chs. 5 and 10.

Any possible unexpectedly high value of $|L|_{\text{rest}}$ has been eliminated by low-pass filtering of the signals. It should also be noted that the entire hemodynamic response for the given 10 s task period is irrelevant to the objective in this paper, because the initial dip in the initial stage of the hemodynamic response has a meaning.

3.2. *Hand-clenching experiment*

The ΔHbO, ΔHbR, ΔHbT, and ΔCOE time series of the activated channels (Chs. 1 to 3) for the entire hand-clenching task for Sub. 1 are provided in Fig. 7. The vector-based phase diagrams of all 12 channels for the first trial are shown in Fig. 8.

Similarly to the mental arithmetic experiment, it can be seen that the vectors corresponding to first few data points appear in the initial dip phases (Cases 3 and 4) showing early deoxygenation and then moving to the conventional stage of increased ΔHbO and decreased ΔHbR. The trajectories in the vector-phase diagrams of the inactive channels remain within the threshold circle, which is determined as the highest value of $|L|$ during the resting state; the vectors below this value, therefore, represent inactivation.

Although initial dips were detected successfully, there was a delay of a few data points (0.8–1 s) after the task period onset. To reduce this delay and to detect it in real time as soon as the task starts, we propose to use a prediction algorithm to forecast the dynamics of the fNIRS signals.

4. Reduction of Time Delay (Prediction)

In order to further reduce the time delay (defined as the time gap between the onset of a task and the time when the initial dip is detected) of the detection of the initial dip, we used a q-step-ahead prediction to pre-determine the occurrence of the initial dip. For this purpose, an autoregressive moving average with exogenous inputs (ARMAX) model for localization and prediction of brain activation prompted by a particular cortical task was used. Although various models including the general linear model have been used frequently in the previous studies,[54–58] they require improvements in the design matrix for the analysis of optical signals.[60]

To estimate and predict the hemodynamic responses mathematically, the following discrete ARMAX model was adopted.[59,60]

$$\begin{aligned}\text{HbX}^i(k) = &\sum_{n=1}^{n_0} a_n^i \text{HbX}^i(k-n) \\ &+ \sum_{m=1}^{m_0} b_m^i \text{dHRF}(k-k_d-m) \\ &+ \sum_{p=1}^{p_0} c_p^i w(k-p) + \varepsilon^i(k),\end{aligned} \tag{6}$$

where HbX denotes the HbO and HbR time series, the superscript i denotes the channel number, k is the discrete time, dHRF denotes the desired hemodynamic response function (i.e. input), w represents

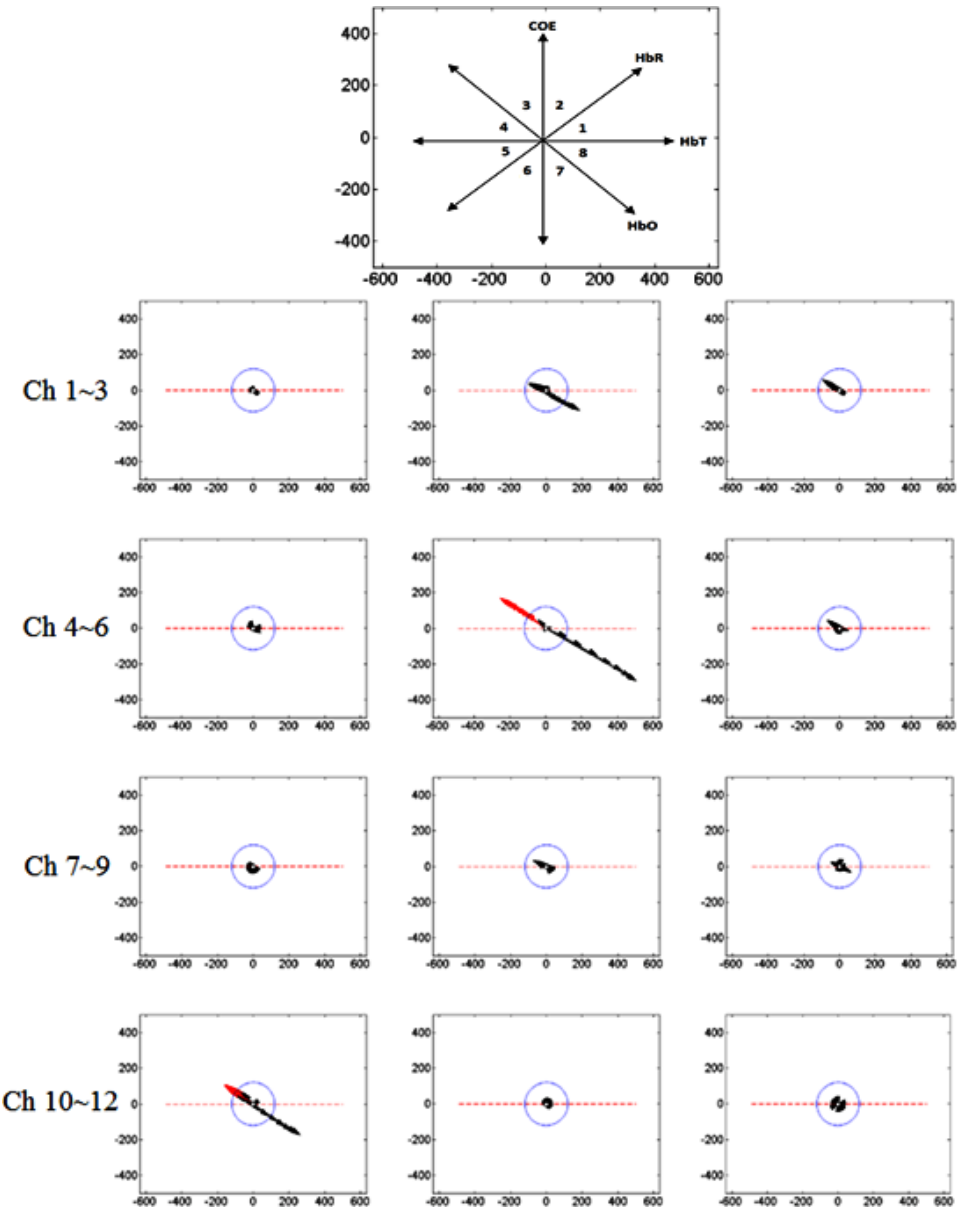

Fig. 6. (Color online) Vector-based phase diagram of all 12 channels for the mental arithmetic task (Sub. 1, trial 1): Chs. 5 and 10 show initial dips marked in red. Vectors of all other channels remain within the threshold circle except Ch. 2 which shows some activation, however, initial dip is not detected in it.

the exogenous signals, and ε is the zero mean Gaussian noise. a_n, b_m, and c_p denote the coefficients of the time series of the system, input, and physiological noise, whereas n, m, and p are their orders, respectively, and k_d is the dead time.

It is noted that, in Eq. (5) of Kamran and Hong,[59] the exogenous signal w included specifically three physiological signals (heartbeat, breathing, Mayer wave) and the baseline correction part.

The dHRF is defined as the convolution of the canonical hemodynamic response function (cHRF), $h(k)$, and the stimulus, $s(k)$, as follows.

$$u(k) = k_1 \sum_{n=0}^{k-1} h(n)s(k-n), \tag{7}$$

where u is the dHRF, k_1 is the scaling parameter used to scale the amplitude of the response (here,

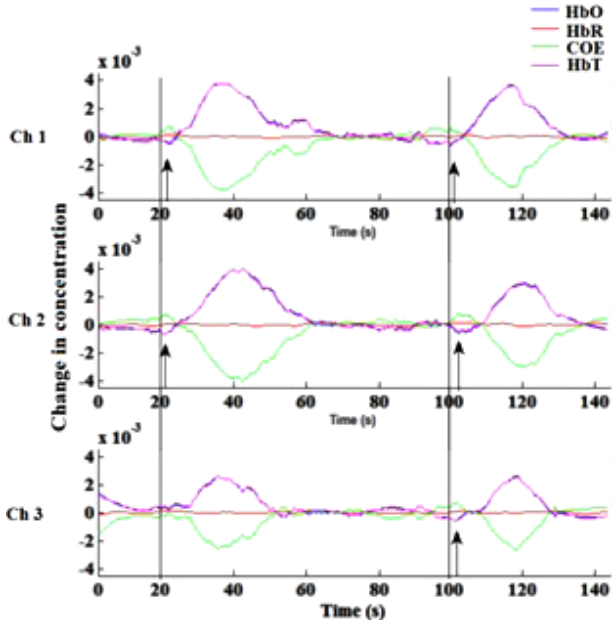

Fig. 7. Time series of ΔHbO, ΔHbR, ΔHbT, and ΔCOE for the hand clinching experiment (Sub. 2). The black lines mark the start of the 20 s task periods whereas the black arrows mark the detection of initial dips.

$k_1 = 10$ was used) if required, and $s(k)$ is defined as

$$s(k) = \begin{cases} 0, & \text{if } k \in \text{rest}, \\ 1, & \text{if } k \in \text{task}, \end{cases} \tag{8}$$

where rest and task stand for the rest and the task periods, respectively. The cHRF, $h(k)$, in Eq. (7) is generated as a linear combination of two Gamma variant functions[55,60] as follows.

$$h(k) = \alpha_1 \left[\frac{(k/\tau_1)^{(\varphi_1 - 1)} e^{-(k/\tau_1)}}{\tau_1(\varphi_1 - 1)!} - \alpha_2 \frac{(k/\tau_2)^{(\varphi_2 - 1)} e^{-(k/\tau_2)}}{\tau_2(\varphi_2 - 1)!} \right], \tag{9}$$

where α_1 is the amplitude, τ_i and φ_i $(i = 1, 2)$ tune the shape and scale, respectively, and α_2 is the ratio of the response to the undershoot (in our work, $\alpha_1 = \alpha_2 = 0.16, \tau_1 = \tau_2 = 1, k = 10, \phi_1 = 6, \phi_2 = 16$ were used).

A simple way to identify the ARMAX model, Eq. (6), is to use a Matlab function armax: Once n, m, and p, and k_d are specified, it returns a_n, b_m, and c_p for given input and output data (in this work, the input was dHRF, and the output was the measured HbX and $n_0 = m_0 = 1$, and $p_0 = k_\mathrm{d} = 0$ were used).

For prediction, the following q-step-ahead prediction model was used, whose structure was determined through Eq. (6).

$$y_p^i(k+q) = \sum_{n=1}^{n_0} a_n^i y_p^i(k+q-n) + \sum_{m=1}^{m_0} b_m^i \mathrm{HbX}^i(k-m) + \sum_{p=1}^{p_0} w(k+q-p) + \varepsilon^i(k), \tag{10}$$

where y_p is the predicted value, q is the prediction step size. The input in this model is the measured hemodynamic response.

The system identification toolbox of Matlab ("armax" and "predict" commands) can be used to implement the prediction part. If an initial dip occurs at around 0.9 s, the maximum horizon for prediction is less than 0.9 s. In the mental arithmetic task, $q = 7$ was used because the sampling frequency of NIRSout was 7.81 Hz. However, in the hand-clenching task, $q = 2$ was used because the used sampling frequency of DYNOT was 1.81 Hz.

The measured and predicted time series of ΔHbO for the mental arithmetic task are plotted in Fig. 9. A vector-phase analysis of the predicted ΔHbO and ΔHbR (or ΔHbT and ΔCOE) signals was performed to determine whether initial dips are detectable using the predicted data or not. It is found that if the estimation model and the prediction model are the same, the *predict* command precedes the data in the forward direction. Since the time information is not visible in the vector-phase analysis plots, to compare the times in which the initial dips were detected in two cases, the HbO magnitudes of the measured (L_m) and predicted data (L_p), representing changes in reaction amplitude, were compared in Fig. 9.

As shown in Fig. 10, the predicted data reflect well the measured data. The instance at which the magnitude of the resultant vectors crosses the threshold line is marked as the start of the initial dip. It can be seen that the start of the initial dip for the predicted data preceded that of the measured data. Since we used 7-step-ahead prediction (∼0.9 s), the initial dip detected using the predicted data can precede that of the measured data up to 0.9 s, if it is successful. At this point, it is

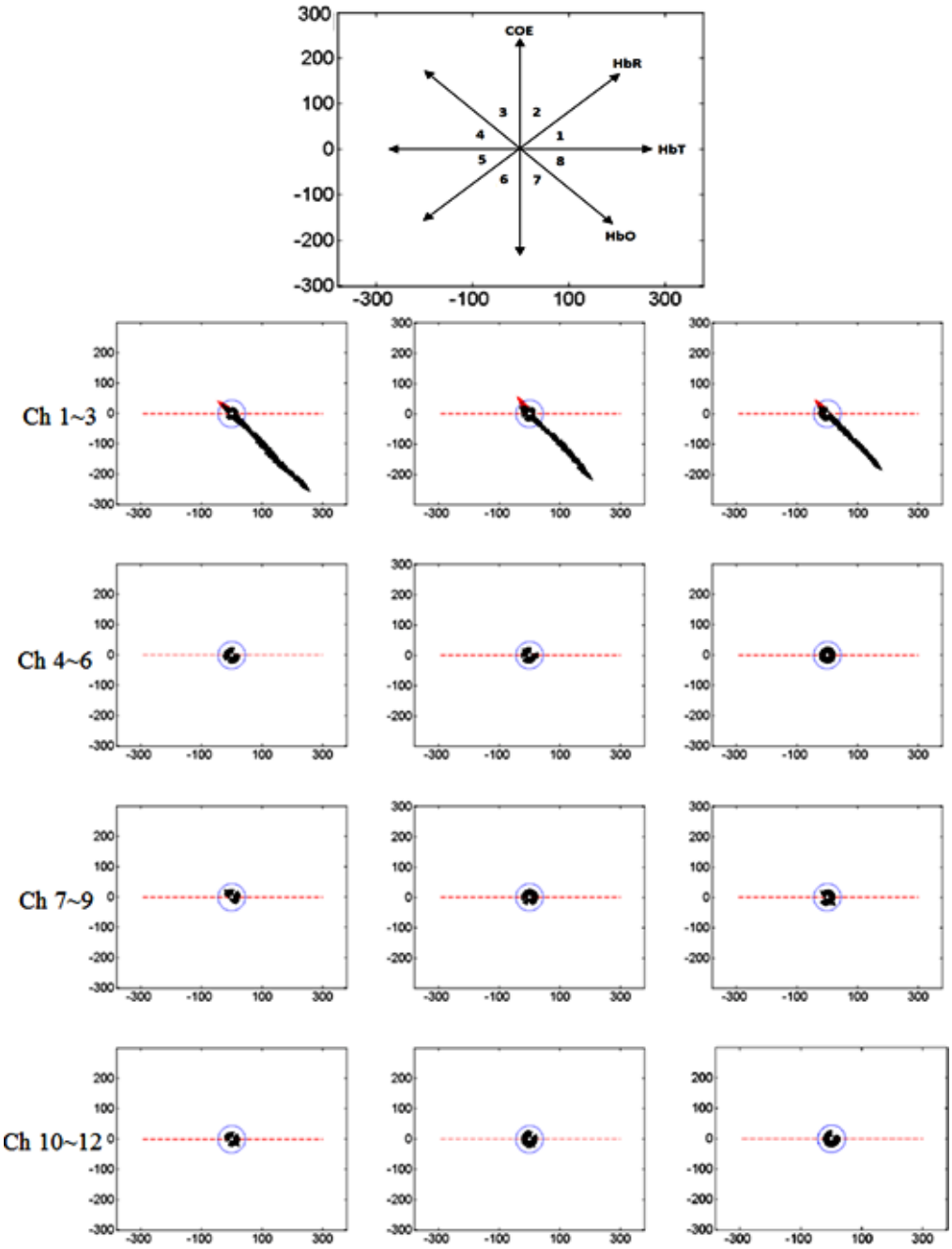

Fig. 8. (Color online) Vector-based phase diagram of all 12 channels for the hand clenching experiment (Sub. 2, trial 2): Chs. 1, 2, and 3 show initial dips marked in red. Vectors of all other channels remain within the threshold circle representing no activation.

noted that ΔCOE and ΔHbT are not measured, but they are computed using the values of ΔHbO and ΔHbR.

The initial dips were detected in 10 signals out of 15 cases for the mental arithmetic task (five trials, three active channels) and in five signals out of six cases from the hand clenching task (two trials, three active channels). The detection times for two experiments are tabulated in Tables 1 and 2, respectively.

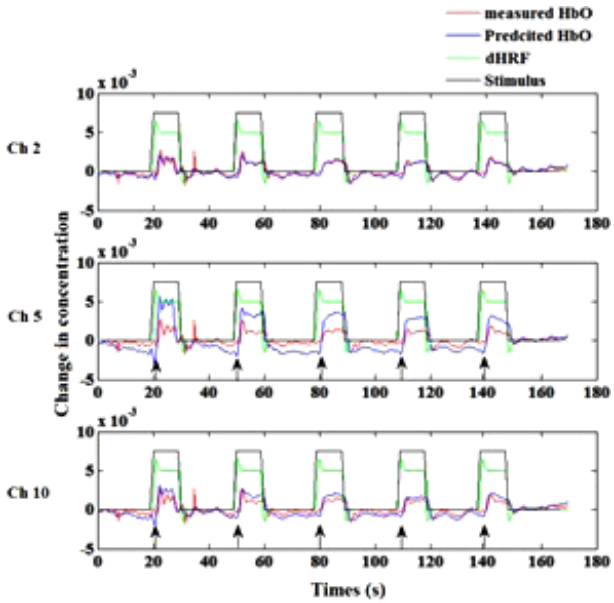

Fig. 9. Comparison of the measured and predicted (7-step ahead) ΔHbOs for the mental arithmetic task (Sub. 1). The stimulation period and the dHRF are also shown. Initial dips detected using the predicted response are marked with arrows.

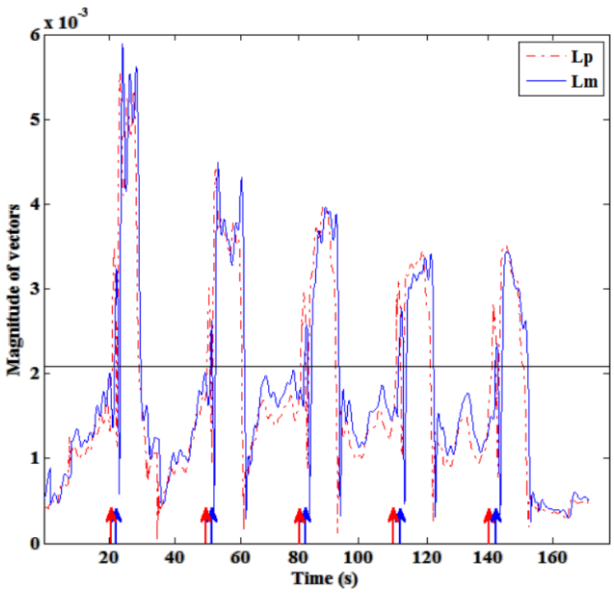

Fig. 10. (Color online) Magnitudes of vectors from measured and predicted data for the mental arithmetic task (Subject 1, Ch. 5): The magnitude of vectors calculated from measured ΔHbO and ΔHbR and the predicted ΔHbO and ΔHbR are shown in blue and red colors, respectively. The constant black line in the middle represents the threshold value given by a circle in the vector-based phase diagram.

Table 1. The measurement time of initial dip for the mental arithmetic task.

Ch	Trial 1	Trial 2	Trial 3	Trial 4	Trial 5
2	Not detected	Not detected	Not detected	Not detected	Not detected
5	0.90 s	0.81 s	0.87 s	0.93 s	0.91 s
10	0.92 s	0.85 s	0.89 s	0.91 s	0.91 s

Table 2. The measurement time of initial dip for the hand-clenching task.

Ch	Trial 1	Trial 2
1	0.91 s	0.93 s
2	0.87 s	0.90 s
3	Not detected	0.90 s

5. Discussion

This paper presents a work on the detection of initial dips from the prefrontal and the primary motor cortices using a threshold value in the vector-based phase diagram to make a decision. An fNIRS time-series prediction method to reduce the detection time of the initial dip is also proposed. The general mathematical formulation of ARMAX exists in the literature. However, the application of ARMAX to a brain-activation estimation model was presented by the author's previous papers.[59,60] Also, the q-step-ahead prediction has been proposed to reduce the time lag. Even though the ARMAX model has been used in the previous study for brain-activation and estimation modeling, the novelty of this study lies in the proposition of adopting the threshold value criterion to make a decision and the utilization of an ARMAX model in the q-step-ahead prediction to reduce the time lag.

In this paper, the use of a threshold circle in the vector-based phase diagram for detecting initial dips is firstly proposed. In this case, the initial dip delay (time lag) is defined as the time gap between the onset of a task and the time when the vector exceeds the threshold circle. In this work, a threshold value for each channel is set to the highest strength (see Sec. 2.1) during the resting state of the channel. Through this, a time delay of approximately less than 1 s can be achieved, while Wylie *et al.*[2] had detected the rising of the hemodynamic response at approximately 2 s after the onset of the task period. This initial dip delay should be further shortened to

enable more fast BCI applications. To reduce further, we developed a q-step-ahead prediction algorithm based on the ARMAX model.

One of the objectives in this paper is to grasp an idea on the amount of reduction time in both cases; by using the vector-based phase analysis and by using the ARMAX model. Therefore, the analyses have been done separately. But, in real applications, both processes should be run in parallel. To quantify the size of initial dip delay (from the start of brain activation), the starting time of external stimulation has been marked. If this happens, it will be a reactive BCI, which means that neuronal commands are made upon external stimuli. But, for active BCI, the occurrence of initial dips should be checked from the baseline signal during the resting state. In this case, the detection time can be further shortened because a visual delay to respond to external stimuli can be avoided. In real-time applications, the ARMAX model should get activated as soon as the fNIRS signals get received and preprocessed.

One of the disadvantages of using fNIRS for BCI purposes was the inherent delay in the conventional hemodynamic response. Now, the detection of the initial dip can enable a faster BCI application.[61–69] Furthermore, it might also allow for more spatially specific brain mapping and, thus, provide insight into neurovascular coupling, because it is believed to be closely related to the region of metabolism.

The vector-based phase analysis method allows for monitoring of changes at the brain-activation level by evaluating four different indices simultaneously. The four indices can be analyzed in the same plane, and their interrelationship can be observed simultaneously. The magnitude of the vectors represents the extent of change in hemoglobin, and can be considered as a new index of brain-activity strength change.[70] Several previous attempts to detect initial dips have focused only on ΔHbR increase, ignoring other possibilities for initial dips in the fNIRS response.[32–34] The vector-based phase analysis enables analyses of brain functionality and initial dip without overlooking several other initial-dip detection possibilities. It also allows the possibility of classifying initial dips into different phases (phases 1 through 4). The feature extraction and classification[71–78] of initial dips can play an important role in the development of initial-dip-based fNIRS-BCIs as well as in detection and diagnosis of several brain disorders.[79–90] For an online BCI,[91–95] the ARMAX model parameters and the threshold values will be estimated during the training stage. The stimulus $s(k)$ in this case remains the same for a synchronous (also called cue-paced) BCI. Notwithstanding these advantages, a disadvantage is that, in the vector-phase analysis, the time information is not evident, and a time-series analysis is required to see the behavior of each index in time.

The ARMAX modeling has been done for both experiments, but only the mental task has been included in the paper. The aim of this paper does not lie in a neuroscientific finding of the differences between the motor cortex and the frontal lobe. Actually, there may not be any difference in the time lags in the motor and prefrontal cortices. The time lag for the motor cortex was also around 0.9 s on average.

Using the threshold values based on the resting-state data, the initial dips were detected in 15 signals out of 21 cases (10/15 from the prefrontal cortex, 5/6 from the motor cortex). No detection in Ch. 2 in Fig. 6 while the signal itself deviated from the circle, for instance, may imply that either the initial dip strength was too small or the channel itself was away from the brain signal source. A better indicator can be proposed in the future. The used prediction algorithm, moreover, was based on fNIRS data represented with a simple ARMA input-output model. An improved prediction algorithm in the future might enable a better prediction, and thereby a better detection of the initial dip.

6. Conclusions

In this paper, a scheme for detecting initial dips in fNIRS signals was investigated. To cope with the latency of hemodynamics, the proposed scheme of combining the vector-based phase analysis, setting a threshold value(s), and the prediction method was proved to be very efficient. The results demonstrated that initial dips can indeed be detected successfully, and also, that the detection time lag can be reduced using an ARMAX model-based q-step-ahead prediction algorithm. To generate different control commands for BCI, initial dips not only can be detected but also can be classified into different phases. In fact, detection of initial dips promises to clear new paths toward better understanding of neurovascular coupling and more spatially specific brain imaging.

Conflict of Interest

The authors declare that they have no conflict of interest. This research was conducted in the absence of any commercial or financial relationship that could be construed as a potential conflict of interest.

Acknowledgments

This work was supported by the National Research Foundation of Korea under the auspices of the Ministry of Science, ICT and Future Planning, Korea (Grant No. NRF-2014R1A2A1A10049727).

References

1. T. Kato, A. Kamei, S. Takashima and T. Ozaki, Human visual cortical function during photic stimulation monitoring by means of near-infrared spectroscopy, *J. Cereb. Blood Flow Metab.* **13** (1993) 516–520.
2. G. R. Wylie, H. L. Graber, G. T. Voelbel, A. D. Kohl, J. DeLuca, Y. Pei, Y. Xu and R. L. Barbour, Using co-variations in the Hb signal to detect visual activation: A near infrared spectroscopic imaging study, *Neuroimage* **47** (2009) 473–481.
3. Y. Hoshi, Functional near-infrared spectroscopy: Current status and future prospects. *J. Biomed. Opt.* **12** (2012) 062106.
4. M. Ferrari and V. Quaresima, A brief review on the history of human functional near-infrared spectroscopy (fNIRS) development and fields of application, *Neuroimage* **63** (2012) 921–935.
5. S. M. Coyle, T. E. Ward, C. M. Markham and G. McDarby, On the suitability of near-infrared (NIR) systems for next generation brain-computer interfaces, *Physiol. Meas.* **25** (2004) 815–822.
6. S. M. Coyle, T. E. Ward and C. M. Markham, Brain-computer interface using a simplified functional near-infrared spectroscopy system, *J. Neural Eng.* **4** (2007) 219–226.
7. M. Naito, Y. Michioka, K. Ozawa, Y. Ito, M. Kiguchi and T. Kanazaw, A communication means for totally locked-in ALS patients based on changes in cerebral blood volume measured with near-infrared light, *IEICE Trans. Inform. Syst.* **90** (2007) 1028–1037.
8. R. Sitaram, H. Zhang, C. Guan, M. Thulasidas, Y. Hoshi, A. Ishikawa, K. Shimizu and N. Birbaumer, Temporal classification of multichannel near-infrared spectroscopy signals of motor imagery for developing a brain-computer interface, *Neuroimage* **34** (2007) 1416–1427.
9. X.-S. Hu, K.-S. Hong, S. S. Ge and M.-Y. Jeong, Kalman estimator- and general linear model-based on-line brain activation mapping by near-infrared spectroscopy, *Biomed. Eng. Online* **9** (2010) 82.
10. X.-S. Hu, K.-S. Hong and S. S. Ge, Recognition of stimulus-evoked neuronal optical response by identifying chaos levels of near-infrared spectroscopy time series, *Neurosci. Lett.* **504**(2) (2011) 115–120.
11. X.-S. Hu, K.-S. Hong and S. S. Ge, fNIRS-based online deception decoding, *J. Neural Eng.* **9**(2) (2012) 026012.
12. X.-S. Hu, K.-S. Hong and S. S. Ge, Reduction of trial-to-trial variations in functional near-infrared spectroscopy signals by accounting for resting-state functional connectivity, *J. Biomed. Opt.* **18**(1) (2013) 017003.
13. S. Moghimi, A. Kushki, S. D. Power, A. M. Guerguerian and T. Chau, Automatic detection of a prefrontal cortical response to emotionally rated music using multi-channel near-infrared spectroscopy, *J. Neural Eng.* **9** (2012) 026022.
14. N. Naseer and K.-S. Hong, Classification of functional near-infrared spectroscopy signals corresponding to right- and left-wrist motor imagery for development of a brain-computer interface, *Neurosci. Lett.* **553** (2013) 84–89.
15. H. Santosa, M. J. Hong, S.-P. Kim and K.-S. Hong, Noise reduction in functional near-infrared spectroscopy signals by independent component analysis, *Rev. Sci. Instrum.* **84**(7) (2013) 073106.
16. H. Santosa, M. J. Hong and K.-S. Hong, Lateralization of music processing with noise in the auditory cortex: An fNIRS study, *Front. Behav. Neurosci.* **8** (2014) 418.
17. M. R. Bhutta, K.-S. Hong, B.-M. Kim, M. J. Hong, Y.-H. Kim and S.-H. Lee, Note: Three wavelengths near-infrared spectroscopy system for compensating the light absorbance by water, *Rev. Sci. Instrum.* **85**(2) (2014) 026111.
18. M. R. Bhutta, M. J. Hong, Y.-H. Kim and K.-S. Hong, Single-trial lie detection using a combined fNIRS-polygraph system, *Front. Psychol.* **6** (2015) 709.
19. K.-S. Hong and H.-D. Nguyen, State-space models of impulse hemodynamic responses over motor, somatosensory, and visual cortices, *Biomed. Opt. Express* **5**(6) (2014) 1778–1798.
20. M. J. Khan, M. J. Hong and K.-S. Hong, Decoding of four movement directions using hybrid NIRS-EEG brain-computer interface, *Front. Hum. Neurosci.* **8** (2014) 244.
21. G. Jasdzewski, G. Strangman, J. Warner, K. K. Kwong, R. A. Poldrack and D. A. Boas, Differences in the hemodynamic response to event-related motor and visual paradigms as measured by near-infrared spectroscopy, *Neuroimage* **20** (2003) 479–488.
22. R. Wang, I. Tsuda and Z. Zhang, A new work mechanism on neuronal activity, *Int. J. Neural Syst.* **25**(3) (2015) 1450037.
23. A. Grinvald, R. D. Frostig, R. M. Siegel and E. Bartfeld, High-resolution optical imaging of functional

brain architecture in the awake monkey, *Proc. Natl. Acad. Sci. U. S. A.* **88** (1991) 11559–11563.
24. D. Malonek and A. Grinvald, Interactions between electrical activity and cortical microcirculation revealed by imaging spectroscopy: Implications for functional brain mapping, *Science* **272** (1996) 551–554.
25. X. Hu and E. Yacoub, The story of the initial dip in fMRI, *Neuroimage* **62**(2) (2012) 1103–1108.
26. M. Jones, J. Berwick, D. Johnston and J. Mayhew, Concurrent optical imaging spectroscopy and laser-Doppler flowmetry: The relationship between blood flow, oxygenation, and volume in rodent barrel cortex, *Neuroimage* **13** (2011) 1002–1015.
27. T. Kato, Principle and technique of NIRS imaging for human brain FORCE: Fast-oxygen response in capillary event, in *Proc. ISBET*, Vol. 1270 (2004), pp. 85–90.
28. T. Kato, Apparatus for evaluating biological function. WO/2003/068070 (2006), Available at http://www.wipo.int/patentscope/search/en/WO2003068070 (Accessed on 10 June 2015).
29. T. Akiyama, T. Ohira, T. Kawase and T. Kato, TMS orientation for NIRS-functional motor mapping, *Brain Topogr.* **19** (2006) 1–9.
30. M. Suh, S. Bahar, A. Mehta and T. Schwartz, Blood volume and hemoglobin oxygenation response following electrical stimulation of human cortex, *Neuroimage* **31** (2006) 66–75.
31. K. Yoshino and T. Kato, Vector-based phase classification of initial dips during word listening using near-infrared spectroscopy, *Neuroreport* **23** (2012) 947–951.
32. T. Ernst and J. Hennig, Observation of a fast response in functional MR, *Magn. Reson. Med.* **3** (1994) 146–149.
33. X. Hu, T. H. Le and K. Ugurbil, Evaluation of the early response in fMRI in individual subjects using short stimulus duration, *Magn. Reson. Med.* **37** (1997) 877–884.
34. D. S. Kim, T. Q. Duong and S. G. Kim, High-resolution mapping of iso-orientation columns by fMRI, *Nat. Neurosci.* **3** (2000) 164–169.
35. M. Watanabe, A. Bartels, J. H. Macke, Y. Murayama and N. K. Logothetis, Temporal jitter of the BOLD signal reveals a reliable initial dip and improved spatial resolution, *Curr. Biol.* **23**(21) (2013) 2146–2150.
36. K. Yoshino, N. Oka, K. Yamamoto, H. Takahashi and T. Kato, Functional brain imaging using near-infrared spectroscopy during actual driving on an express-way, *Front. Hum. Neurosci.* **7** (2013) 882.
37. K. Yoshino, N. Oka, K. Yamamoto, H. Takahashiand and T. Kato, Correlation of prefrontal cortical activation with changing vehicle speeds in actual driving: A vector-based functional near-infrared spectroscopy study, *Front. Hum. Neurosci.* **7** (2013) 895.
38. T. Kato, Biofunction diagnosis device, biofunction diagnosis method, bioprobe, bioprobe wearing tool, bioprobe support tool, and bioprobe wearing assisting tool, WO/2006/009178 (2007), Available at http://www.wipo.int/patentscope/search/en/WO2006009178 (Accessed on 10 June 2015).
39. B. Christie, Doctors revise Declaration of Helsinki, *BMJ* **321**(7266) (2000) 913.
40. S. D. Power, T. H. Falk and T. Chau, Classification of prefrontal activity due to mental arithmetic and music imagery using hidden Markov models and frequency domain near-infrared spectroscopy, *J. Neural Eng.* **7**(2) (2010) 026002.
41. S. D. Power, A. Kushki and T. Chau, Towards a system-paced near-infrared spectroscopy brain-computer interface: Differentiating prefrontal activity due to mental arithmetic and mental singing from the no-control state, *J. Neural Eng.* **8** (2011) 066004.
42. S. D. Power, A. Kushki and T. Chau, Automatic single trial discrimination of mental arithmetic, mental singing and the no-control state from the prefrontal activity: Towards a three-state NIRS-BCI, *BMC Res. Notes* **5** (2012) 141.
43. S. D. Power, A. Khushki and T. Chau, Intersession consistency of single-trial classification of the prefrontal response to mental arithmetic and the no-control state by NIRS, *PLoS ONE* **7**(7) (2012) e37791.
44. K.-S. Hong, N. Naseer and Y.-H. Kim, Classification of prefrontal and motor cortex signals for three-class fNIRS-BCI, *Neurosci. Lett.* **587** (2015) 87–92.
45. N. Naseer and K.-S. Hong, fNIRS-based brain-computer interfaces: A review, *Front. Hum. Neurosci.* **9** (2015) 3.
46. N. Naseer and K.-S. Hong, Decoding answers to four-choice questions using functional near-infrared spectroscopy, *J. Near Infrared Spectrosc.* **23**(1) (2015) 23–31.
47. N. Naseer, M. J. Hong and K.-S. Hong, Online binary decision decoding using functional near-infrared spectroscopy for the development of a brain-computer interface, *Exp. Brain Res.* **232**(2) (2014) 555–564.
48. P. W. McCormick, M. Stewart, G. Lewis, M. Dujovny and J. I. Ausman, Intracerebral penetration of infrared light: technical note, *J. Neurosurg.* **76** (2007) 315–318.
49. G. Gratton, C. R. Brumback, B. A. Gordon, M. A. Pearson, K. A. Low and M. Fabiani, Effects of measurement method, wavelength, and source-detector distance on the fast optical signal, *Neuroimage* **32** (2006) 1576–1590.
50. Q. Zhang, E. N. Brown and G. E. Strangman, Adaptive filtering to reduce global interference in evoked brain activity detection: A human subject case study, *J. Biomed. Opt.* **12** (2007) 064009.

51. B. D. Frederick, L. D. Nickerson and Y. Tong, Physiological denoising of BOLD fMRI data using regressor interpolation at progressive time delays (RIPTiDe) processing of concurrent fMRI and near-infrared spectroscopy (NIRS), *Neuroimage* **60** (2012) 1913–1923.
52. L. Gagnon, M. A. Yucel, M. Dehaes, R. J. Cooper, K. L. Perdue, J. Selb, T. J. Huppert, R. D. Hoge and D. A. Boas, Quantification of the cortical contribution to the NIRS signal over the motor cortex using concurrent NIRS-fMRI measurements, *Neuroimage* **59** (2012) 3933–3940.
53. L. Kocsis, P. Herman and A. Eke, The modified Beer-Lambert law revisited, *Phys. Med. Biol.* **51** (2006) N91–N98.
54. S. Ferdowsi, S. Sanei and V. Abolghasemi, A predictive modeling approach to analyze data in EEG-fMRI experiments, *Int J. Neural Syst.* **25**(1) (2015) 1440008.
55. M. M. Plichta, S. Heinzel, A. C. Ehlis, P. Pauli and A. J. Fallgatter, Model-based analysis of rapid event-related functional near-infrared spectroscopy (NIRS) data: A parametric validation study, *Neuroimage* **35**(2) (2007) 625–634.
56. M. Gouko and K. Ito, An action generation model by using time series prediction and its applications to robot navigation, *Int. J. Neural Syst.* **19**(2) (2009) 105–113.
57. E. Kirilina, A. Jelzow, A. Heine, M. Niessing, H. Wabnitz, R. Bruhl, B. Itterman, A. M. Jacobs and I. Tachtsidis, The physiological origin of task-evoked systemic artefacts in functional near infrared spectroscopy, *Neuroimage* **61**(1) (2012) 70–81.
58. S. Tak and J. C. Ye, Statistical analysis of fNIRS data: A comprehensive review, *Neuroimage* **85** (2014) 72–91.
59. M. A. Kamran and K.-S. Hong, Reduction of physiological effects in fNRS waveform for efficient brain-state decoding, *Neurosci. Lett.* **580** (2014) 130–136.
60. M. A. Kamran and K.-S. Hong, Linear parameter varying model and adaptive filtering technique for detecting neuronal activities: An fNIRS study, *J. Neural Eng.* **10** (2013) 056002.
61. M. A. Lopez-Gordo, F. Pelayo, A. Prieto and E. Fernandez, An auditory brain-computer interface with accuracy prediction, *Int. J. Neural Syst.* **22**(3) (2012) 1250009.
62. J. Jin, E. W. Sellers, S. Zhou, Y. Zhang, X. Wang and A. Cichocki, A P300 brain-computer interface based on a modification of the mismatch negativity paradigm, *Int. J. Neural Syst.* **25**(3) (2015) 1550011.
63. A. Ortiz-Rosario and H. Adeli, Brain-computer interface technologies: From signal to action, *Rev. Neurosci.* **24**(5) (2013) 537–552.
64. A. Ortiz-Rosario, I. Berrios-Torres, H. Adeli and J. A. Buford, Combined corticospinal and reticulospinal effects on upper limb muscles, *Neurosci. Lett.* **561** (2014) 30–34.
65. A. Burns, H. Adeli and J. A. Buford, Brain-computer interface after nervous system injury, *Neuroscientist* **20**(6) (2014) 639–651.
66. A. Ortiz-Rosario, H. Adeli and J. A. Buford, Wavelet methodology to improve single unit isolation in primary motor cortex cells, *J. Neurosci. Methods* **246** (2015) 106–118.
67. Y. Zhang, G. Zhou, J. Jin, Q. Zhao, X. Wang and A. Cichocki, Aggregation of sparse linear discriminant analyses for event-related potential classification in brain-computer interface, *Int. J. Neural Syst.* **24**(1) (2014) 1450003.
68. J. Li, H. Ji, L. Cao, D. Zang, R. Gu and B. Xia, Evaluation and application of a hybrid brain computer interface for real wheelchair control with multi-degrees of freedom, *Int. J. Neural Syst.* **24**(4) (2014) 1450014.
69. M. Nakanishi, Y. Wang, Y. T. Wang, Y. Mitsukura and T. P. Jung, A high-speed brain speller using steady-state visual evoked potentials, *Int. J. Neural Syst.* **24**(6) (2014) 1450019.
70. M. Sano, S. Sano, N. Oka, K. Yoshino and T. Kato, Increased oxygen load in the prefrontal cortex from mouth breathing: A vector-based near-infrared spectroscopy study, *Neuroreport* **24** (2013) 935–940.
71. Y. Liu, Q. Zhao and L. Zhang, Uncorrelated multiway discriminant analysis for motor imagery EEG classification, *Int. J. Neural Syst.* **25**(4) (2015) 155.
72. K. Jackowski, B. Krawczyk and M. Wozniak, Improved adaptive splitting and selection: The hybrid training method of a classifier based on a feature space partitioning, *Int. J. Neural Syst.* **24**(3) (2014) 1430007.
73. Q. Yuan, W. Zhou, S. Yuan, X. Li, J. Wang and G. Jia, Epileptic EEG classification based on kernel sparse representation, *Int. J. Neural Syst.* **24**(4) (2014) 1450015.
74. O. Reyes, C. Morell and S. Ventura, Evolutionary feature weighting to improve the performance of multi-label lazy algorithms, *Integr. Comput.-Aided Eng.* **21**(4) (2014) 339–354.
75. Y. Yu and T. McKelvey, A robust subspace classification scheme based on empirical intersection removal and sparse approximation, *Integr. Comput.-Aided Eng.* **22**(1) (2015) 59–69.
76. D. Kim, S. Rho and E. Hwang, Classification and indexing scheme of large-scale image repository for spatio-temporal landmark recognition, *Integr. Comput.-Aided Eng.* **22**(2) (2015) 201–213.
77. L. F. S. Coletta, E. R. Hruschka, A. Acharya and J. Ghosh, Using metaheuristics to optimize the combination of classifier and cluster ensembles, *Integr. Comput.-Aided Eng.* **22**(3) (2015) 229–242.
78. J. Jin, B. Z. Allison, Y. Zhang, X. Wang and A. Cichocki, An ERP-based BCI using an oddball

paradigm with different faces and reduced errors in critical functions, *Int. J. Neural Syst.* **24**(8) (2014) 1450027.
79. H. Adeli, S. Ghosh-Dastidar and N. Dadmehr, Alzheimer's disease and models of computation: Imaging, classification, and neural models, *J. Alzheimers Dis.* **7**(3) (2005) 187–199.
80. H. Adeli, S. Ghosh-Dastidar and N. Dadmehr, Alzheimer's disease: Models of computation and analysis of EEGs, *Clin. EEG Neurosci.* **36**(3) (2005) 131–140.
81. H. Adeli, S. Ghosh-Dastidar and N. Dadmehr, A spatio-temporal wavelet-chaos methodology for EEG-based diagnosis of Alzheimer's disease, *Neurosci. Lett.* **444**(2) (2008) 190–194.
82. M. Ahmadlou, H. Adeli and A. Adeli, New diagnostic EEG markers of the Alzheimer's disease using visibility graph, *J. Neural Transm.* **117**(9) (2010) 1099–1109.
83. A. Ahmadlou, H. Adeli and A. Adeli, Fractality and a Wavelet-Chao methodology for EEG-based diagnosis of Alzheimer's disease, *Alzheimer Dis. Assoc. Disord.* **25**(1) (2011) 85–92.
84. Z. Sankari and H. Adeli, Probabilistic neural networks for EEG-based diagnosis of Alzheimer's disease using conventional and wavelet coherence," *J. Neurosci. Methods* **197**(1) (2011) 165–170.
85. Z. Sankari, H. Adeli and A. Adeli, Intrahemispheric, interhemispheric and distal EEG coherence in Alzheimer's disease, *Clin. Neurophysiol.* **122**(5) (2011) 897–906.
86. Z. Sankari, H. Adeli and A. Adeli, Wavelet coherence model for diagnosis of Alzheimer's disease, *Clin. EEG Neurosci.* **43**(3) (2012) 268–278.
87. M. Ahmadlou, A. Adeli, R. Bajo and H. Adeli, Complexity of functional connectivity networks in mild cognitive impairment patients during a working memory task, *Clin. Neurophisiol.* **125**(4) (2014) 694–702.
88. M. Ahmadlou and H. Adeli, Fuzzy synchronization likelihood with application to attention-deficit/hyperactivity disorder, *Clin. EEG Neurosci.* **42**(1) (2011) 6–13.
89. M. Ahmadlou, H. Adeli and A. Adeli, Fractality analysis of frontal brain in major depressive disorder, *Int. J. Psychophysiol.* **85**(2) (2012) 206–211.
90. M. Ahmadlou, H. Adeli and A. Adeli, Spatio-temporal analysis of relative convergence (STARC) of EEGs reveals differences between brain dynamics of depressive women and men, *Clin. EEG Neurosci.* **44**(3) (2013) 175–181.
91. M. J. Khan and K.-S. Hong, Passive BCI based on drowsiness detection: An fNIRS study, *Biomed. Opt. Express* **6**(10) (2015) 4063–4078.
92. L. A. Farwell and E. Donchin, Talking off the top of your head: Toward a mental prosthesis utilizing event-related brain potentials, *Electroenceph. Clin. Neurophysiol.* **70** (1988) 510–523.
93. J. J. Vidal, Towards direct brain-computer communication, *Annu. Rev. Biophys. Bioeng.* **2** (1973) 157–180.
94. J. J. Vidal, Real-time detection of brain events in EEG, *Proc. IEEE* **65** (1977) 633–664.
95. S. Bozinovski, M. Sestakov and L. Bozinovska, Using EEG alpha rhythm to control a mobile robot, in *Proc. 10th Ann. Conf. Society of IEEE Eng. in Med. Biol.*, Vol. 3 (1988), pp. 1515–1516.